Biosensors and Bioelectronics 144 (2019) 111660

Contents lists available at ScienceDirect

Biosensors and Bioelectronics

journal homepage: www.elsevier.com/locate/bios

Ultrasensitive detection of miRNA-155 based on controlled fabrication of AuNPs@MoS_2 nanostructures by atomic layer deposition

Lei Liu*,[1], Songyang Zhu[1], Yumin Wei, XiaoLin Liu, Songlong Jiao, Junjie Yang

Jiangsu Key Laboratory for Design and Manufacture of Micro-Nano Biomedical Instruments, School of Mechanical Engineering, Southeast University, Nanjing, 211189, People's Republic of China

ARTICLE INFO

Keywords:
ALD
MoS_2
MiRNA-155
Electrochemical platform

ABSTRACT

MicroRNA-155 (miRNA-155) is a typical cancer-related biomarker, which often exists at ultralow concentrations in the plasma or body fluids of early patients. In this work, a novel label-free platform for ultrasensitive miRNA-155 detection was designed based on the precise fabrication of molybdenum disulfide (MoS_2) by atomic layer deposition (ALD). Au nanoparticles (AuNPs)@MoS_2 nanostructures were the core parts for the detection electrode, and the measurement precision of the sensing platform was modulated and optimized by ALD-based thickness and shape control of ultrathin MoS_2 nanoflakes (thickness: ~14 nm, about 20 layers, uniform continuous distribution). In the detection experiment, MoS_2 nanoflakes served as a conductive skeleton to support more AuNPs, and the results showed that the effective control of their morphology and thickness was of vital importance for ultrasensitive acquisition of detection signals. With using toluidine blue (TB) as a hybridization indicator, ultrasensitive detection record ranging from 1 fM to 10 nM with a detection limit of 0.32 fM can be achieved.

1. Introduction

MiRNAs are one kind of the most important biomarkers, which play a significant role in regulating cell differentiation, proliferation and apoptosis (Engels and Hutvagner, 2006; He and Hannon, 2004; Zhao et al., 2010; Bi et al., 2015). As a typical one, the aberrant expression of miRNA-155 in serum or plasma can be regarded as a critical assay index for certain cancers such as nonsmall cell lung cancer, breast cancer and B-cell lymphoma (Faraoni et al., 2009; Jiang et al., 2010; Heegaard et al., 2012). Ultrasensitive, rapid and accurate detections for miRNA are highly desirable for the early diagnosis of kinds of cancers (Shuai et al., 2016; Kong et al., 2014). For example, nanomaterials such as AuNPs (Wang et al., 2015a), Ag nanoclusters (Miao et al., 2018) and multi-walled carbon nanotube-gold nanocomposites (MWCNT/AuNCs) (Ma et al., 2018) have been reported as fluorescence quenching platform for miRNA detection. Different strategies such as recyclable surface-enhanced Raman spectroscopy (SERS) (Wu et al., 2018; Mohammadniaei et al., 2018), MoS_2-based field-effect transistor (FET) (Majd et al., 2018), electrochemiluminescence (Zhang et al., 2018) were developed for miRNA-155 detection. Besides, colorimetric method also presented high sensitivity and selectivity for miRNA analysis in biological samples (Li et al., 2016). But limitations of various detection methods (Valoczi et al., 2004; Kilic et al., 2018; Silahtaroglu et al., 2007; Li and Ruan, 2009), such as heavy workload, long time-consuming, expensiveness and high sample-consuming, still need special attentions and further in-depth studies (Turner, 2013; Wang et al., 2015b; Rafiee-Pour et al., 2016).

Two-dimensional (2D) materials seem more attractive for electrochemical analysis (Jamali et al., 2014; Conde et al., 2015; Geim and Novoselov, 2007). As a typical representative, MoS_2 is considered to have lower electronic conductivity compared with carbon nanomaterials (Chhowalla et al., 2013). Therefore, the functionalization of MoS_2 by noble metal nanoparticles can accelerate the electron transfer, produce synergistic effect and enlarge further applications (Wang et al., 2017; Mao et al., 2017). Li-intercalation exfoliation and microwave-assisted hydrothermal method were employed to prepare AuNPs-decorated MoS_2 nanosheets for the dual-mode electrochemical detection of miRNA-21 (Su et al., 2017). Similar preparation methods were also used to synthesize the MoS_2-thionine-AuNPs nanohybrids to achieve miRNA-21 detection (Zhu et al., 2017). Although various traditional manufacturing methods (Su et al., 2014, 2016) have been used for fabricating MoS_2 and its nanocomposites (Maitra et al., 2012; Lee et al., 2012; Li et al., 2003), the size, thickness control, uniform distribution, manufacturing efficiency and repeatability still remain challenging.

* Corresponding author.
E-mail address: liulei@seu.edu.cn (L. Liu).
[1] These authors contributed equally to this work.

https://doi.org/10.1016/j.bios.2019.111660
Received 19 May 2019; Received in revised form 7 August 2019; Accepted 27 August 2019
Available online 29 August 2019
0956-5663/

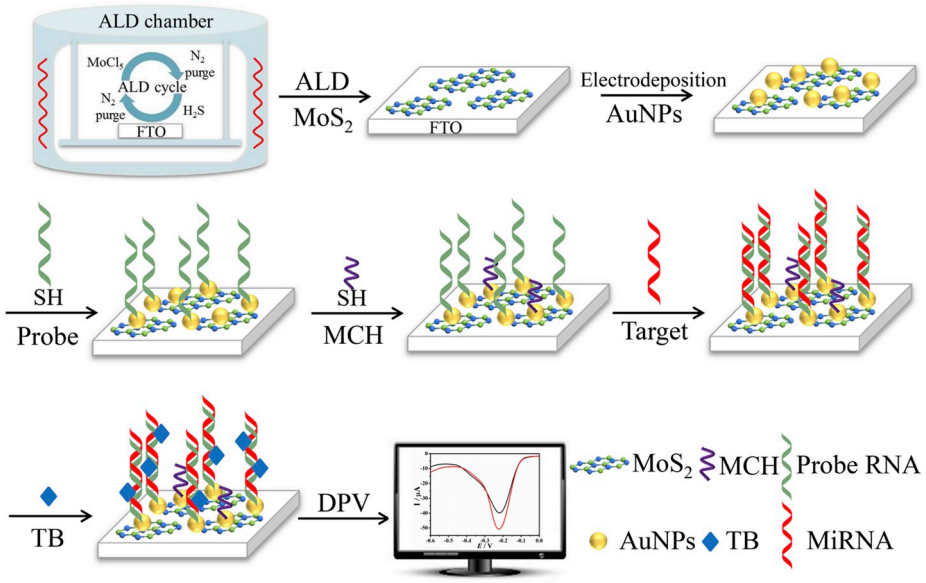

Fig. 1. Fabrication steps of miRNA sensing platform and detection principle.

Obviously, high sensitivity, instant detection feedback and good specificity put forward higher requirements for the manufacture of MoS_2. Due to the high surface energy and Van der Waals interactions, inherent stacking feature of MoS_2 nanosheets decreases the exposed active sites, reduces the specific surface area and greatly weakens the electrochemical performance (Zheng et al., 2014). To prevent the agglomeration of MoS_2 nanosheets, AuNPs/hollow MoS_2 microcubes was also synthesized for miRNA-21 detection, but the material preparation method, requirements for the experimental conditions and enzyme activity were more complex and stringent (Shuai et al., 2017). By contrast, ALD has been widely used to obtain uniform and conformal films with accurate size and thickness controlled by self-limiting reaction. It is a new way to achieve iultrathin MoS_2 with high efficiency and repeatability (Tan et al., 2014; Jang et al., 2016). Recently, ALD has been used as a significant design strategy of nanostructures for electrocatalysis, energy storage and environmental applications (Marichy et al., 2012; Bechelany et al., 2015), but it has been rarely developed for electrochemical biosensors (Raza et al., 2019; Wei et al., 2019).

In this work, a novel label-free electrochemical platform for miRNA-155 ultrasensitive detection was fabricated based on ALD-made AuNPs@MoS_2 nanostructures with using TB as a hybridization indicator, related sensing sensitivity and mechanism were under discussion.

2. Experimental

2.1. Chemicals and materials

FTO electrode was obtained from Guluo glass Co. LTD (Luoyang, China). Molybdenum chloride ($MoCl_5$), hydrogen tetrachloroaurate trihydrate ($HAuCl_4{\cdot}3H_2O$), 6-mercaptohexanol (MCH), phosphate-buffer solution (PBS), toluidine blue (TB), potassium hexacyanoferrate-III ($K_3[Fe(CN)_6]$) and potassium hexacyanoferrate-II ($K_4[Fe(CN)_6]$) trihydrate were purchased from Sigma-Aldrich (Shanghai, China). Hydrogen sulfide (H_2S), Oxygen (O_2) and Nitrogen (N_2) were supplied by Nanjing Special Gas Co.Ltd (Nanjing, China). The oligonucleotimde sequences were provided by Sangon Biotech Co. Ltd (Shanghai, China) and their sequences were as follows:

Probe SH-RNA: 5′–SH–ACC CCU AUC ACG AUU AGC AUU AA-3′
MiRNA-155: 5′-UUA AUG CUA AUC GUG AUA GGG GU-3′
Single-base mismatch: 5′-UUA AGG CUA AUC GUG AUA GGG GU-3′
MiRNA-21: 5′-UAG CUU AUC AGA CUG AUG UUG A-3′

All solutions were prepared with diethylpyrocarbonate-treated water to reduce the effect of RNase on the experimental results.

2.2. Techniques

Electrochemical measurements were performed on an electrochemical workstation (CHI660E, Shanghai Chenhua Instruments, China) with a conventional three-electrode system composed of a modified FTO (0.25 cm^2) as working electrodes, a saturated calomel electrode as reference electrodes and a platinum wire as counter electrode. The morphologies and chemical elements of nanostructures were characterized by scanning electron microscope (SEM) and energy dispersive spectroscopy (EDS) (Inspect F50, FEI, USA). Crystal structures were observed by X-ray diffraction (XRD, Smartlab-3, Rigaku, USA), Raman spectra (RAM-PRO-785E, Agiltron, USA). The thicknesses and microstructures of modified electrode were measured by atomic force microscopy (AFM, MicroNano D-5A, Zhuolun MicroNano, China). A commercial ALD setup (SUNALETMR-100, PICOSUN, Finland) was employed for the deposition of MoS_2 films.

2.3. In-situ growth of MoS_2 films

Bare FTO substrate was cleaned sequentially using sonication for 20 min in acetone, ethanol, and deionized water and dried under N_2 flow. After washed, FTO substrate was treated with O_2 plasma for 5 min. The schematic process for obtaining ALD-made MoS_2 was shown in Fig. 1, in which the temperature of ALD chamber was controlled at 450 ˚C and the pressure was controlled at 5.3 hundred Pa (hPa). Mo precursor was $MoCl_5$ and its source bottle was kept at 200 ˚C. H_2S was kept at room temperature with a base pressure of 8 hPa. N_2 was set at a flow rate of 50 standard cubic-centimeter per minute (sccm) to pulse and purge $MoCl_5$ and H_2S into ALD chamber alternately. The cleaned FTO substrate was placed in ALD chamber and experienced the following two self-limiting reactions:

(A) $Mo\text{-}SH^* + MoCl_5 \rightarrow Mo\text{–}S\text{–}MoCl_4 + HCl$;
(B) $MoCl^* + H_2S \rightarrow Mo\text{-}SH^* + HCl + S$.

The samples containing MoS_2 grown in-situ on FTO by 10-, 20-, 30-, 40-, 50- and 70-ALD cycles were named as 10-MoS_2/FTO, 20-MoS_2/FTO, 30-MoS_2/FTO, 40-MoS_2/FTO, 50-MoS_2/FTO and 70-MoS_2/FTO, respectively.

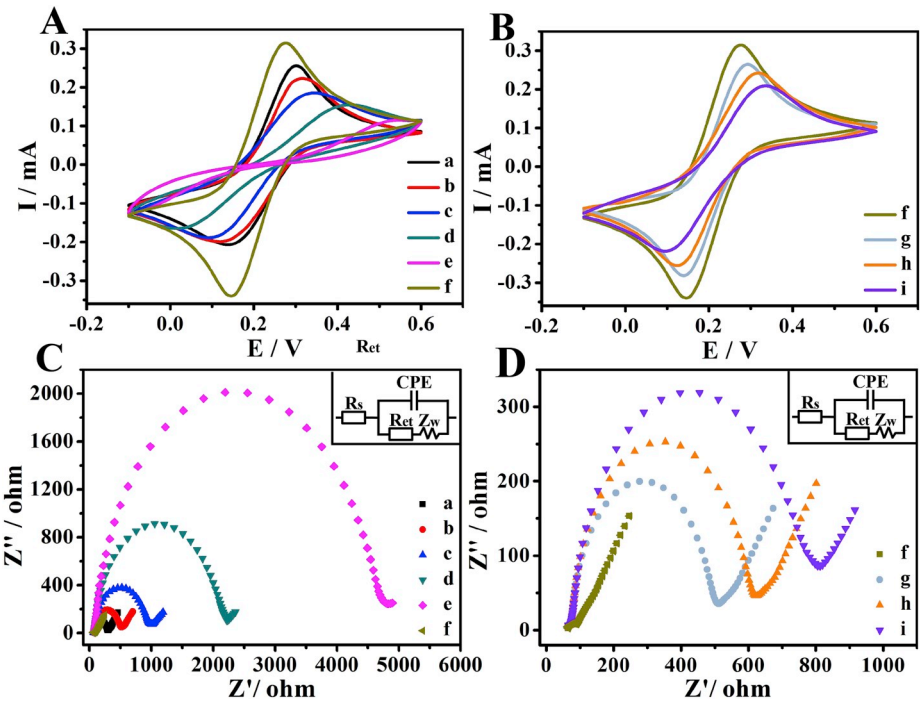

Fig. 2. CVs (A, B) and EIS (C, D) of bare FTO (a), 10-MoS_2/FTO (b), 30-MoS_2/FTO (c), 50-MoS_2/FTO (d), 70-MoS_2/FTO (e), AuNPs/30-MoS_2/FTO (f), SH-RNA/AuNPs/30-MoS_2/FTO (g), MCH/SH-RNA/AuNPs/30-MoS_2/FTO (h), miRNA/MCH/SH-RNA/AuNPs/30-MoS_2/FTO (i) in 5 mmol L^{-1} $[Fe(CN)_6]^{3-/4-}$ containing 0.1 mol L^{-1} KCl solution. The schematic of equivalent circuit (inset in C, D) was consisted of solution resistance (Rs), electron-transfer resistance (Ret), constant-phase element (CPE), and Warburg impedance (Zw).

2.4. Sensing platform based on AuNPs@MoS_2

To assemble probe thiolated RNA (SH-RNA), AuNPs were electrodeposited on MoS_2/FTO electrode in a solution containing 0.1 mol L^{-1} KNO_3 and 0.1% $HAuCl_4$ solution at a constant potential of −0.2 V for 300 s (room temperature). Then, 15 μL of SH-RNA solution (1 μM) was dropped onto the surface of AuNPs/MoS_2/FTO electrode and kept at room temperature for 6h, namely SH-RNA/AuNPs/MoS_2/FTO. After gently rinsed with PBS to remove unbound probe SH-RNA, 20 μL of MCH solution (1 mM) was added on SH-RNA/AuNPs/MoS_2/FTO for 60 min to fill unreacted Au sites (named as MCH/SH-RNA/AuNPs/MoS_2/FTO) and eliminate nonspecific adsorption. Again, the electrode was washed, and 15 μL of miRNA-155 with different concentrations was applied on the electrode and incubated at 37 °C for 120 min. Thus, miRNA/MCH/SH-RNA/AuNPs/MoS_2/FTO electrode was obtained after thoroughly washed to remove unhybridized oligonucleotides.

For targets sensing, cyclic voltammetry (CV) were carried out in 5 mmol L^{-1} $[Fe(CN)_6]^{3-/4-}$ containing 0.1 mol L^{-1} KCl solution between − 0.1 V and 0.6 V. Electrochemical impedance spectroscopy (EIS) measurements were performed in 5.0 mmol L^{-1} $[Fe(CN)_6]^{3-/4-}$ and 0.1 mol L^{-1} KCl solution from 100 kHz to 0.1 Hz. Differential pulse voltammetry (DPV) measurements were carried out after the miRNA/MCH/SH-RNA/AuNPs/MoS_2/FTO electrode immersed into TB solution (20 μM TB-0.2M NaCl-PBS pH 7.4) for 5 min.

3. Results and discussion

3.1. Precise fabrication of sensing platform by ALD

The principle of miRNA sensing platform was illustrated in Fig. 1. By using ALD, the thickness, size and distribution of the MoS_2 nanoflakes on electrode surface can be controlled in-situ. Functionalized AuNPs@MoS_2 nanostructures were obtained by subsequent electrodeposition of AuNPs to solve the limitations such as lower electronic conductivity of MoS_2 and stable binding of probe RNA. The existence of the 2H phase of MoS_2 was confirmed by Raman spectra (Fig. S1A), and XRD patterns demonstrated the successful fabrication of AuNPs@MoS_2 nanostructures for the sensing platform (Fig. S1B). From the subsequent experimental results, in-situ growth of MoS_2 nanoflakes by ALD was anchored throughout the surface of FTO electrode uniformly, served as a conductive skeleton with large specific surface area to support more AuNPs and exerted synergistic effect for amplifying detection signals. SH-RNA was used as a probe which can match complementary target miRNA-155 via hydrogen bonding and fixed on AuNPs/MoS_2/FTO electrode through Au–S bond. MCH was used to fill unreacted Au sites and eliminated nonspecific adsorption of the modified electrode.

The selection of a suitable hybridization indicator is of great importance for obtaining a sensing platform with high sensitivity and specificity. TB is a phenothiazine dye and employed as the hybridization indicator in this work to achieve label-free detection of miRNA-155. Different methods have been reported to study the interaction of TB with nucleotide sequence (Paul and Kumar, 2013; Jiao et al., 2005; Chen et al., 2003), but its application as a hybridization indicator for the electrochemical detection of miRNA has rarely been approached. Due to the π-π conjugated electrons, TB has good compatibility with RNA. TB is able to enhance its stability to binding to single-stranded and double-stranded nucleic acid sequences by electrostatic and hydrogen bonding. Compared with the electrostatic adsorption of TB to single-stranded RNA, it also enhances binding to double-stranded RNA by intercalation, which exhibits that double-stranded RNA has better affinity with TB than single-stranded RNA (Tian et al., 2018). Therefore, after the modified electrode was immersed into TB solution for 5 min, more TB would accumulate on the surface of modified electrode by electrostatic and hydrogen bonding (Nguyen et al., 2016), where the probe RNA matched the high concentration of target miRNA-155. By contrast, the addition of low concentrations of miRNA-155 or mismatched RNA to the modified electrode reduced the amount of TB that bound to the double-stranded RNA by intercalation, which can be employed to effectively discriminate different concentrations and matched RNA. Then, when DPV measurements were performed from 0 V to −0.6 V, TB exhibited the following redox reaction on the electrode surface:

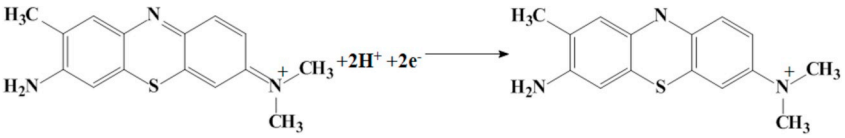

Finally, the reduction current of TB was reflected by DPV, and the ultrasensitive label-free detection of miRNA-155 was achieved from the subsequent experimental results.

The validity of the step-by-step modification of the sensing platform can be verified from the change of redox peak in 5 mM $[Fe(CN)_6]^{3-/4-}$ solution. Fig. 2A showed that MoS_2/FTO electrode exhibited a lower current redox peak of $[Fe(CN)_6]^{3-/4-}$ and wider peak potential difference with ALD cycles increasing (**curve b-curve e**) than bare FTO (**curve a**), mainly because more MoS_2 with low electronic conductivity grown on the FTO electrode surface. However, the current response increased obviously after AuNPs were further assembled on the MoS_2/FTO electrode by electrodeposition (**curve f**), which indicated MoS_2 nanoflakes can support AuNPs with excellent electrical conductivity to exert synergistic effect and accelerate the electron transfer. In addition, Fig. 2B showed the decrease of the current redox peak for the construction of sensing platform. When SH-RNA was immobilized (**curve g**), current response decreased because the oligonucleotides were non-conductive. After MCH was attached to the electrode (**curve h**), the current response was further decreased because MCH filled unreacted Au sites and resulted in the difficult electron transferring. Similarly, after immobilization of target miRNA (**curve i**), the current response was further decreased due to the more difficult electron transfer after target miRNA being hybridized with SH-RNA. EIS was measured to reflect detailed changes in charge-transfer resistance (Ret) and the values of Ret were calculated from the equivalent circuit. Fig. 2C showed the increase diameter of the semicircle can illustrate the enhancement in interfacial Ret. Ret value of the bare FTO was about 68.5Ω (**curve a**) and increased with in-situ grown of MoS_2 with low conductivity on the FTO surface after different ALD cycles (**curve b-e**). The detailed values of Ret for 10-MoS_2/FTO, 30-MoS_2/FTO, 50-MoS_2/FTO and 70-MoS_2/FTO were 121.6Ω, 231.1Ω, 517.2Ω and 1118.7Ω, respectively. After AuNPs were coated on the MoS_2/FTO, Ret decreased significantly to 45.2Ω and exhibited an almost straight line (**curve f**), mainly because of improvement of the electron transfer by AuNPs. As shown in Fig. 2D, Ret obviously increasesd to 119Ω after SH-RNA fixed on AuNPs/30-MoS_2/FTO electrode through Au–S bond (**curve g**). When MCH were then applied on electrode, Ret increased to 147.5Ω, because MCH obstructed the electron transfer between modified electrodes and solution (**curve h**). Finally, Ret increased to 183.4Ω and the sensing platform was completed after miRNA was applied (**curve i**). These results corresponded to the changes in CVs and the successful construction of the sensing platform can be confirmed.

3.2. Measurement precision control based on ALD

The oxidation peak of CV measurements were selected for assessing the optimum performance of AuNPs/MoS2/FTO platform. The current signal was increased with the reaction cycles from 0 to 30 and then decreased after more ALD cycles (Fig. 3A). Particularly, AFM images and height profiles of 30-MoS_2/FTO sample indicated that the thickness of 30-MoS_2 nanoflakes was ~14 nm (inserted image in Fig. 3A), which was about 20 layers based on the thickness (0.65 nm) of the single-layer MoS_2. Therefore, it was possible to adjust MoS_2 nanoflakes by ALD to acquire the optimum current signal, since a certain amount of MoS_2 exhibited a higher specific surface area, which provided active sites for electrodeposition of AuNPs and exerted synergistic effect for accelerating the electron transfer. But, the agglomeration and stacking of thickened MoS_2 obstructed electron transfer and reduced active sites for AuNPs, which was also verified by the subsequent experiment (Fig. 4). On the other hand, the current signal increased with the deposition time of AuNPs from 100 s to 300 s and then almost stayed stable after 300 s (Fig. S2A), mainly because of saturation of deposited AuNPs on 30-MoS_2/FTO. The current signal decreased with the hybridization time increasing and then remained almost unchanged after 120 min (Fig. S2B). Besides, the binding degree of probe RNA and miRNA-155 was affected by the incubation temperature. The current signal decreased with the incubation temperature increasing and then increased slowly after 37 °C, which was near the normal human body temperature (Fig. S2C). Thus, 30 ALD cycles, 300 s of deposition time, 120 min of hybridization time and 37 °C of incubation temperature were the parameters adopted in the following detection.

Under the same parameters and experiment operation, AuNPs/30-MoS_2/FTO presented an obvious and higher ΔI compared to the AuNPs/FTO without MoS_2 decorated and other AuNPs/MoS_2/FTO samples from different ALD cycles (Fig. 3B). In addition, DPV curves further proved the detailed information about effective signal amplification of AuNPs modified MoS_2 nanoflakes (inserted image in Fig. 3B). AuNPs/30-MoS_2/FTO exhibited the significantly increased reduction peak and ΔI compared with others, which can be attributed to the fact that 30-MoS_2 was more conducive to the deposition of AuNPs to bind more probe RNA for effective signal amplification. Then, more TB was

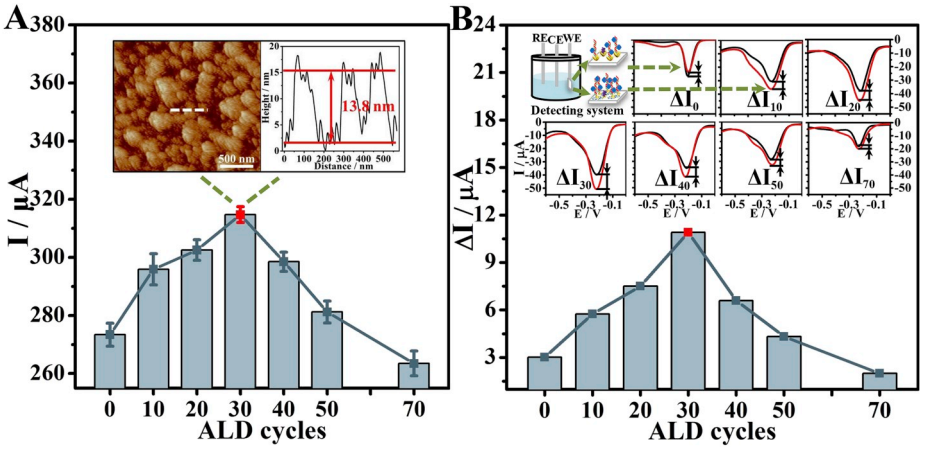

Fig. 3. (A) Influence of the number of ALD cycles on oxidation peak current. Inset: AFM images and height profiles of 30-MoS_2/FTO. (B) Influence of the number of ALD cycles on the differences of the current values ΔI. (ΔI = I_0–I, where I_0 and I represent the reduction peak currents of TB from DPV measurement before and after hybridization with miRNA, respectively). Inset: detecting system composing of a modified FTO as working electrodes (WE), a saturated calomel electrode as reference electrodes (RE) and a platinum wire as counter electrode (CE); DPV curves of the AuNPs/FTO AuNPs/10-MoS_2/FTO, AuNPs/20-MoS_2/FTO, AuNPs/30-MoS_2/FTO, AuNPs/40-MoS_2/FTO, AuNPs/50-MoS_2/FTO, AuNPs/70-MoS_2/FTO before and after hybridization with 1 nM miRNA-155. The ΔI resulted from different ALD cycles were named as ΔI_0, ΔI_{10}, ΔI_{20}, ΔI_{30}, ΔI_{40}, ΔI_{50} and ΔI_{70}, respectively.

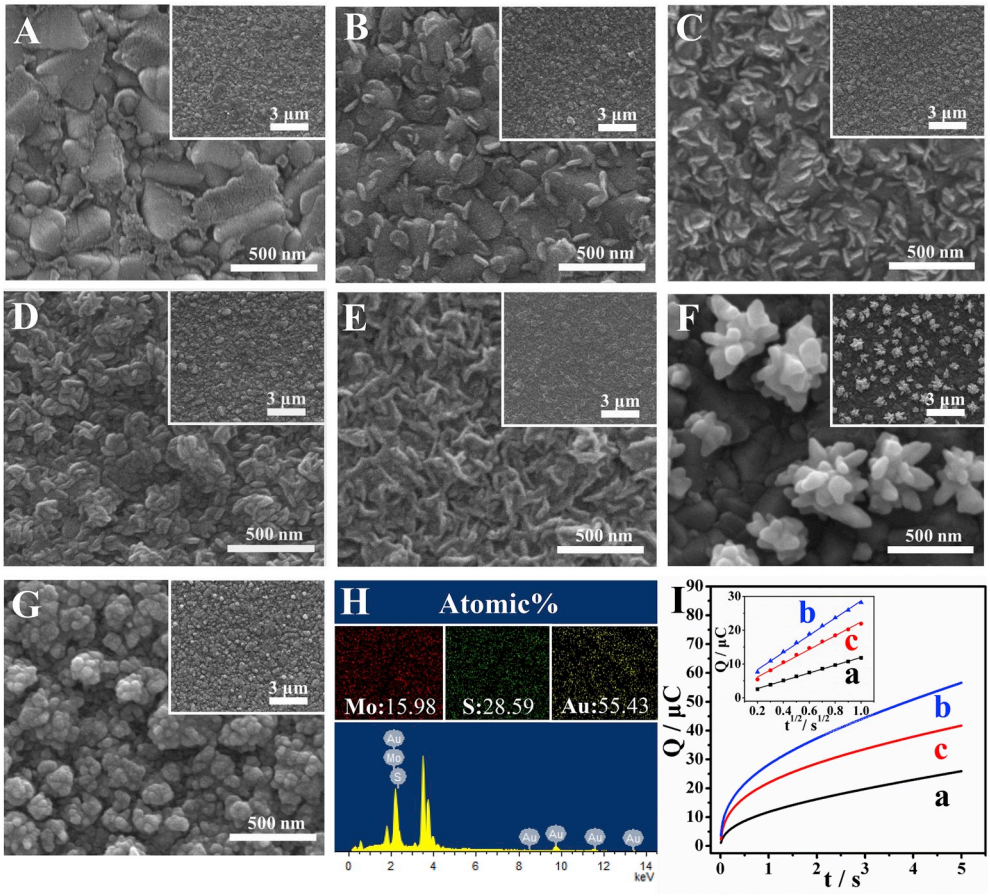

Fig. 4. SEM images of bare FTO (A), 10-MoS_2/FTO (B), 30-MoS_2/FTO (C), 50-MoS_2/FTO (D), 70-MoS_2/FTO (E), AuNPs/FTO (F) and AuNPs/30-MoS_2/FTO (G). (H) Elemental maps and EDS spectrum of AuNPs/30-MoS_2/FTO. (I) Q-t curves of AuNPs/FTO (a), 30-MoS_2/FTO (b) and AuNPs/30-MoS_2/FTO (c). Inset: Q-$t^{1/2}$ curves of AuNPs/FTO (a), 30-MoS_2/FTO (b) and AuNPs/30-MoS_2/FTO (c).

gathered on the surface of modified electrode due to the increased matched target miRNA, which can be utilized to detect lower concentrations of miRNA to acquire optimum detection sensitivity.

The signal amplification of AuNPs@MoS_2 nanostructures was analyzed from a microscopic perspective. Bare FTO surface (Fig. 4A) was irregular and indicated distinct polygonal structures. After the reaction by ALD, large-area uniform MoS_2 nanoflakes distributed directly on the surface of FTO (Fig. 4B-**4C** and the inserted image) can be observed and their size and distribution increased from 10 to 30 ALD cycles. The crystallite size of MoS_2 was larger and exhibited a stacking morphology after 50 cycles (Fig. 4D). For 70-MoS_2/FTO (Fig. 4E), the wrinkle feature was observed in the excess MoS_2 nanoflakes and appeared to become highly textured with out-of-plane orientation.

Thus, from the experimental point of view, large-area uniform and conformal MoS_2 nanoflakes with different thickness were grown in-situ on the surface of FTO electrode and its size, thickness and distribution can be adjusted by layer-by-layer deposition and the self-limiting of ALD. Then, well dispersed MoS_2 nanoflakes supported the subsequent deposition of AuNPs to obtain functionalized AuNPs@MoS_2 nanostructures. Besides, from the detection itself, the incomplete coverage of MoS_2 on the electrode surface reduced exposed active sites for supporting AuNPs to immobilize probe RNA and limited the detection sensitivity. On the other hand, excessive agglomeration of MoS_2 with lower electronic conductivity reduced specific surface area, affected conductivity and detection accuracy of the electrode (Huang et al., 2014), which was consistent with the electrochemical performance in Fig. 3. Fig. 4F showed the agglomerated dendritic gold structures were scattered on FTO without MoS_2 coating after electrodeposition time of 300 s. By contrast, it was obvious that a large number of small and dense AuNPs were assembled on 30-MoS_2/FTO at the same electrodeposition time (Fig. 4G). Here MoS_2 nanoflakes not only served as a conductive skeleton for the sensing platform construction, but also had a higher specific surface area for supporting abundant AuNPs to obtain uniform and dense nanostructures. Furthermore, the elemental maps and EDS spectrum (Fig. 4H) confirmed the existence of Mo, S and Au, in which Au was the most abundant (atomic percentage: 55.43%). In addition, the atomic percentage of Mo and S were 15.98% and 28.59%, respectively, which was close to 1: 2 and consistent with the molecular formula of MoS_2 as well.

The effective surface area of AuNPs/FTO, 30-MoS_2/FTO and AuNPs/30-MoS_2/FTO modified electrodes were tested by chronocoulometry in 0.1 mM $K_3[Fe(CN)_6]$ solution with 1.0 M KCl (Fig. 4I) and can be estimated by followed equation (Anson, 1964):

$$Q = 2nFAcD^{1/2}t^{1/2}/\pi^{1/2} + Q_{dl} + Q_{ads}$$

where n is the number of electrons involved in reaction (n = 1 for $K_3[Fe(CN)_6]$), A (cm^2) is the effective surface area of the working electrode, D ($cm^2 s^{-1}$) is diffusion coefficient ($D = 7.6 \times 10^{-6}\ cm^2\ s^{-1}$ for $K_3[Fe(CN)_6]$ at 25 °C), Q_{dl} (C) is double layer charge and Q_{ads} (C, existence in adsorption process) and other symbols represent their usual meaning. A was obtained by the slope of the linear relation equation of Q-$t^{1/2}$ (inserted image in Fig. 4I). AuNPs/FTO electrode had an effective area of 0.38 cm^2 (**curve a**), which was larger than geometric area of the bare FTO electrode (0.25 cm^2), mainly because of the irregular structure of the electrode surface and the deposited agglomerated dendritic gold nanostructures. By contrast, the effective area of the AuNPs/30-MoS_2/FTO electrode was significantly increased to 0.68 cm^2 (**curve c**), indicating the MoS_2 nanoflakes can serve as a conductive skeleton with larger surface area to support more AuNPs and increase the electron conductivity. Moreover, 30-MoS_2/FTO electrode exhibited the maximum effective surface area of 0.85 cm^2 (**curve c**), which proved indirectly that ALD-made MoS_2 had a large specific surface area and the effective surface area decreased after supporting dense AuNPs.

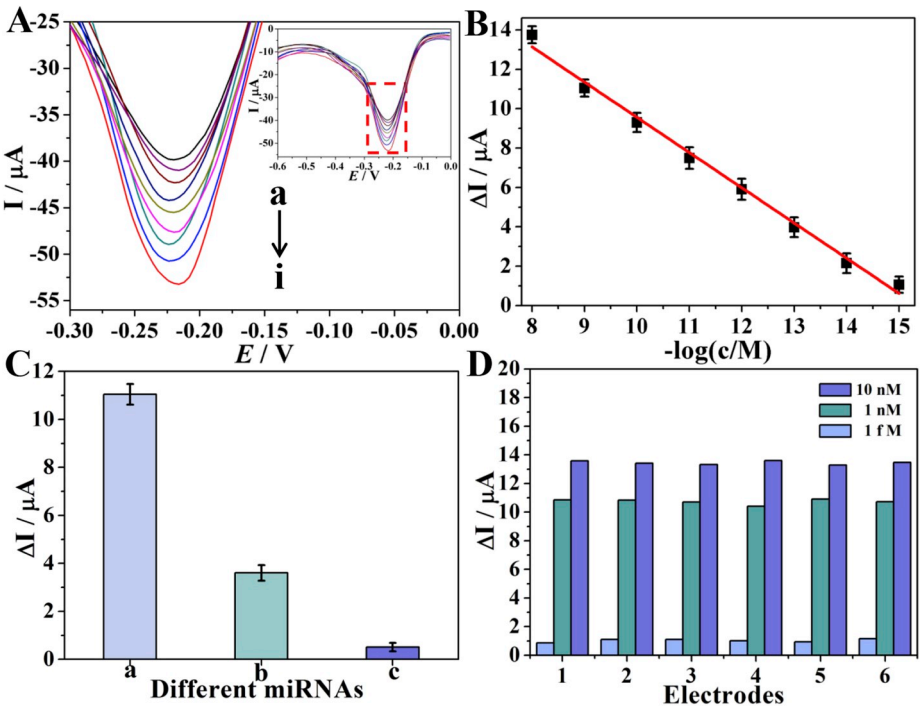

Fig. 5. (A) DPV responses to different concentrations of miRNA-155 from (a) to (i): 0 M, 1×10^{-15} M, 1×10^{-14} M, 1×10^{-13} M, 1×10^{-12} M, 1×10^{-11} M, 1×10^{-10} M, 1×10^{-9} M and 1×10^{-8} M. (B) The relationship between the average of ΔI and the positive logarithm of the different miRNA concentrations from five equally prepared electrodes, respectively. Error bars = standard deviations (n = 5). (C) The selectivity of the sensing platform hybridized to 1 nM miRNA-155 (a), single-base mismatch miRNA (b) and miRNA-21(c). (D) DPV responses of six equally prepared electrodes for 1 fM, 1 nM and 10 nM miRNA-155 detections.

Table 1
Comparison between our strategy and other methods for miRNA-155 detection.

Sequences	Materials	Analytical Methods	Linear range(M)	Detection limit(M)	References
1	Nano-Pd	CV	5.6×10^{-12}-5.6×10^{-5}	1.87×10^{-12}	Wu et al. (2013)
2	MWCNT/AuNPs	Fluorescent	1×10^{-13}-1×10^{-9}	3.34×10^{-14}	Ma et al. (2018)
3	PbS/CdS QD	SWV	5×10^{-14}-3×10^{-11}	1.2×10^{-14}	Zhu et al. (2014)
4	Au/Gra	DPV	1×10^{-14}-1×10^{-9}	3.3×10^{-15}	Wu et al. (2014)
5	CdS/Mn NCs	ECL	5×10^{-15}-5×10^{-10}	1.67×10^{-15}	Peng et al. (2017)
6	GO/GNR	DPV	2×10^{-15}-8×10^{-12}	6×10^{-16}	Azimzadeh et al. (2016)
7	Fe_3O_4@PDA/Pt	SERS	1×10^{-15}-1×10^{-5}	2.8×10^{-16}	Wu et al. (2018)
[a]	**AuNPs@MoS_2**	**DPV**	**1×10^{-15}-1×10^{-8}**	**3.2×10^{-16}**	**This work**

[a] This work exhibited wider linear range and lower detection limit than sequences: 1–6 in the table and achieved more simple and rapid detection with similar detection limit than sequence: 7. (SWV: square wave voltammetry; ECL: electrochemiluminescence).

3.3. Ultrasensitive miRNA-155 detection

The concentration of miRNA-155 was detected ranging from 1 fM to 10 nM. Fig. 5A showed that peak currents increased with miRNA-155 concentration increasing, which was attributed to the reduction current of more TB gathering on the surface of modified electrode.

The calibration curve obtained from five independent experiments' peak current values had a good linear relationship between ΔI and the logarithm of the concentration of miRNA (Fig. 5B): ΔI (μA) = 27.45 + 1.79log(c/M) with correlation coefficient R^2 = 0.99212 and detection limit was 0.32 fM with signal to noise ratio of 3.

Fig.5C showed that higher ΔI was obtained with complementary target miRNA-155 than single-base mismatch miRNA and miRNA-21 at a concentration of 1 nM respectively, which indicated that this platform had high selectivity for complementary target miRNA-155. Moreover, reproducibility was also an important feature of the biosensor. Benefiting from the highly controllable, repeatable and productive ALD process, the relative standard deviations (RSD) were less than 5% for six equally prepared electrodes (Fig.5D) and the error bars in Fig.5B also demonstrated good reproducibility for other concentrations of miRNA-155. The proposed sensing platform was compared with other reported results for miRNA-155 detection in Table 1.

3.4. Stability and serum sample analysis

Long-term stability is an important parameter for the practical application of the biosensor. The modified electrodes were kept under 4 °C for 0–10 days and retained 88.4% of the initial responses to 1 nM miRNA-155, suggesting the proposed platform had good stability (Fig. S3). The practicability of the sensing platform in real sample was evaluated by standard addition method, where four different concentrations of miRNA-155 were added into human serum to obtain a series of samples. As listed in Table S1, the recovery was ranging from 94.33% to 103.30% and the RSD was less than 5%, indicating that our ALD-made sensing platform had a potential analytical application in real biological samples.

4. Conclusion

In summary, a novel label-free electrochemical platform for miRNA-155 ultrasensitive detection has been successfully developed based on combining the ALD-made MoS_2 and electrodeposition of AuNPs. In-situ growth of well dispersed MoS_2 nanoflakes had higher specific surface area for supporting more AuNPs to immobilize oligonucleotides and exerted synergistic effect for amplifying the detection signals. TB was employed as a hybridization indicator and presented efficient current

signals for the label-free detection of miRNA-155 from 1 fM to 10 nM with a low detection limit of 0.32 fM. Therefore, the proposed sensing platform exhibited excellent performance in sensitivity, specificity and reproducibility for miRNA-155 detection. The strategy of utilizing and combining ALD technique with electrodeposition for the construction of sensing platform may be of certain value for the further development of biosensors and draw more attention to further explore the potential applications of ALD technique.

CRediT authorship contribution statement

Lei Liu: Conceptualization, Formal analysis, Funding acquisition, Investigation, Writing - review & editing. **Songyang Zhu:** Formal analysis, Data curation, Writing - original draft. **Yumin Wei:** Investigation. **XiaoLin Liu:** Methodology. **Songlong Jiao:** Investigation. **Junjie Yang:** Formal analysis.

Declaration of competing interest

The authors declare that they have no known competing financial interests or personal relationships that could have appeared to influence the work reported in this paper.

Acknowledgments

This work is financially supported by the National Natural Science Foundation of China (51822501), the Natural Science Funds for Distinguished Young Scholar of Jiangsu Province(BK20170023) the grants from Top 6 High-Level Talents Program of Jiangsu Province (2017-GDZB-006, Class A).

Appendix A. Supplementary data

Supplementary data to this article can be found online at https://doi.org/10.1016/j.bios.2019.111660.

References

Anson, F.C., 1964. Anal. Chem. 36 (4), 932–934.
Azimzadeh, M., Rahaie, M., Nasirizadeh, N., Ashtari, K., Naderi-Manesh, H., 2016. Biosens. Bioelectron. 77, 99–106.
Bechelany, M., Balme, S., Miele, P., 2015. Pure Appl. Chem. 87 (8), 751–758.
Bi, S., Chen, M., Jia, X.Q., Dong, Y., 2015. Nanoscale 7 (8), 3745–3753.
Chen, L.H., Nie, Y.T., Liu, L.Z., Shen, H.X., 2003. Anal. Lett. 36 (1), 107–122.
Chhowalla, M., Shin, H.S., Eda, G., Li, L.J., Loh, K.P., Zhang, H., 2013. Nat. Chem. 5 (4), 263–275.
Conde, J., Edelman, E.R., Artzi, N., 2015. Adv. Drug Deliv. Rev. 81, 169–183.
Engels, B.M., Hutvagner, G., 2006. Oncogene 25 (46), 6163–6169.
Faraoni, I., Antonetti, F.R., Cardone, J., Bonmassar, E., 2009. Biochim. Biophys. Acta 1792 (6), 497–505.
Geim, A.K., Novoselov, K.S., 2007. Nat. Mater. 6 (3), 183–191.
He, L., Hannon, G.J., 2004. Nat. Rev. Genet. 5 (7), 522–531.
Heegaard, N.H.H., Schetter, A.J., Welsh, J.A., Yoneda, M., Bowman, E.D., Harris, C.C., 2012. Int. J. Cancer 130 (6), 1378–1386.
Huang, K.J., Zhang, J.Z., Liu, Y.J., Wang, L.L., 2014. Sens. Actuators B Chem. 194, 303–310.
Jamali, A.A., Pourhassan-Moghaddam, M., Dolatabadi, J.E.N., Omidi, Y., 2014. Trac. Trends Anal. Chem. 55, 24–42.
Jang, Y., Yeo, S., Lee, H.B.R., Kim, H., Kim, S.H., 2016. Appl. Surf. Sci. 365, 160–165.
Jiang, S., Zhang, H.W., Lu, M.H., He, X.H., Li, Y., Gu, H., Liu, M.F., Wang, E.D., 2010. Can. Res. 70 (8), 3119–3127.
Jiao, K., Li, Q.J., Sun, W., Wang, Z.J., 2005. Electroanalysis 17 (11), 997–1002.
Kilic, T., Erdem, A., Ozsoz, M., Carrara, S., 2018. Biosens. Bioelectron. 99, 525–546.
Kong, W., He, L., Richards, E.J., Challa, S., Xu, C.X., Permuth-Wey, J., Lancaster, J.M., Coppola, D., Sellers, T.A., Djeu, J.Y., Cheng, J.Q., 2014. Oncogene 33 (6), 679–689.
Lee, Y.H., Zhang, X.Q., Zhang, W.J., Chang, M.T., Lin, C.T., Chang, K.D., Yu, Y.C., Wang, J.T.W., Chang, C.S., Li, L.J., Lin, T.W., 2012. Adv. Mater. 24 (17), 2320–2325.
Li, W., Ruan, K.C., 2009. Anal. Bioanal. Chem. 394 (4), 1117–1124.
Li, W.J., Shi, E.W., Ko, J.M., Chen, Z.Z., Ogino, H., Fukuda, T., 2003. J. Cryst. Growth 250 (3–4), 418–422.
Li, R.D., Yin, B.C., Ye, B.C., 2016. Biosens. Bioelectron. 86, 1011–1016.
Ma, H., Xue, N., Li, Z.B., Xing, K., Miao, X.M., 2018. Sens. Actuators B Chem. 266, 221–227.
Maitra, U., Matte, H.S.S.R., Kumar, P., Rao, C.N.R., 2012. Chimia 66 (12), 941–948.
Majd, S.M., Salimi, A., Ghasemi, F., 2018. Biosens. Bioelectron. 105, 6–13.
Mao, S., Chang, J.B., Pu, H.H., Lu, G.H., He, Q.Y., Zhang, H., Chen, J.H., 2017. Chem. Soc. Rev. 46 (22), 6872–6904.
Marichy, C., Bechelany, M., Pinna, N., 2012. Adv. Mater. 24 (8), 1017–1032.
Miao, X.M., Cheng, Z.Y., Ma, H.Y., Li, Z.B., Xue, N., Wang, P., 2018. Anal. Chem. 90 (2), 1098–1103.
Mohammadniaei, M., Yoon, J., Lee, T., Choi, J.W., 2018. J. Biotechnol. 274, 40–46.
Nguyen, K.V., Holade, Y., Minteer, S.D., 2016. ACS Catal. 6 (4), 2603–2607.
Paul, P., Kumar, G.S., 2013. Spectroc. Acta Pt. A-Molec. 107, 303–310.
Peng, L.C., Zhang, P., Chai, Y.Q., Yuan, R., 2017. Anal. Chem. 89 (9), 5036–5042.
Rafiee-Pour, H.A., Behpour, M., Keshavarz, M., 2016. Biosens. Bioelectron. 77, 202–207.
Raza, M.H., Movlaee, K., Wu, Y.L., El-Refaei, S.M., Karg, M., Leonardi, S.G., Neri, G., Pinna, N., 2019. ChemElectroChem 6 (2), 383–392.
Shuai, H.L., Huang, K.J., Chen, Y.X., Fang, L.X., Jia, M.P., 2017. Biosens. Bioelectron. 89, 989–997.
Shuai, H.L., Huang, K.J., Xing, L.L., Chen, Y.X., 2016. Biosens. Bioelectron. 86, 337–345.
Silahtaroglu, A.N., Nolting, D., Dyrskjot, L., Berezikov, E., Moller, M., Tommerup, N., Kauppinen, S., 2007. Nat. Protoc. 2 (10), 2520–2528.
Su, S., Cao, W.F., Liu, W., Lu, Z.W., Zhu, D., Chao, J., Weng, L.X., Wang, L.H., Fan, C.H., Wang, L.H., 2017. Biosens. Bioelectron. 94, 552–559.
Su, S., Sun, H.F., Cao, W.F., Chao, J., Peng, H.Z., Zuo, X.L., Yuwen, L.H., Fan, C.H., Wang, L.H., 2016. ACS Appl. Mater. Interfaces 8 (11), 6826–6833.
Su, S., Zhang, C., Yuwen, L.H., Chao, J., Zuo, X.L., Liu, X.F., Song, C.Y., Fan, C.H., Wang, L.H., 2014. ACS Appl. Mater. Interfaces 6 (21), 18735–18741.
Tan, L.K., Liu, B., Teng, J.H., Guo, S.F., Low, H.Y., Tan, H.R., Chong, C.Y.T., Yang, R.B., Loh, K.P., 2014. Nanoscale 6 (22) 14002-14002.
Tian, L., Qian, K., Qi, J., Liu, Q.Y., Yao, C., Song, W., Wang, Y.H., 2018. Biosens. Bioelectron. 99, 564–570.
Turner, A.P.F., 2013. Chem. Soc. Rev. 42 (8), 3184–3196.
Valoczi, A., Hornyik, C., Varga, N., Burgyan, J., Kauppinen, S., Havelda, Z., 2004. Nucleic Acids Res. 32 (22), e175.
Wang, Y.H., Huang, K.J., Wu, X., 2017. Biosens. Bioelectron. 97, 305–316.
Wang, W., Kong, T., Zhang, D., Zhang, J., Cheng, G.S., 2015a. Anal. Chem. 87 (21), 10822–10829.
Wang, X., Nan, F., Zhao, J., Yang, T., Ge, T., Jiao, K., 2015b. Biosens. Bioelectron. 64, 386–391.
Wei, Z.H., Hai, Z.Y., Akbari, M.K., Zhao, Z.T., Sun, Y.J., Hyde, L., Verpoort, F., Hu, J., Zhuiykov, S., 2019. Electrochim. Acta 297, 417–426.
Wu, X.Y., Chai, Y.Q., Yuan, R., Su, H.L., Han, J., 2013. Analyst 138 (4), 1060–1066.
Wu, X.Y., Chai, Y.Q., Yuan, R., Zhuo, Y., Chen, Y., 2014. Sens. Actuators B Chem. 203, 296–302.
Wu, Y.G., He, Y., Yang, X., Yuan, R., Chai, Y.Q., 2018. Sens. Actuators B Chem. 275, 260–266.
Zhang, Y., Li, X., Xu, Z.Q., Chai, Y.Q., Wang, H.J., Yuan, R., 2018. Chem. Commun. 51 (72), 10148–10151.
Zhao, H., Shen, J., Medico, L., Wang, D., Ambrosone, C.B., Liu, S., 2010. PLoS One 5 (10), e13735.
Zheng, X.L., Xu, J.B., Yan, K.Y., Wang, H., Wang, Z.L., Yang, S.H., 2014. Chem. Mater. 26 (7), 2344–2353.
Zhu, D., Liu, W., Zhao, D.X., Hao, Q., Li, J., Huang, J.X., Shi, J.Y., Chao, J., Su, S., Wang, L.H., 2017. ACS Appl. Mater. Interfaces 9 (41), 35597–35603.
Zhu, W.Y., Su, X.P., Gao, X.Y., Dai, Z., Zou, X.Y., 2014. Biosens. Bioelectron. 53, 414–419.